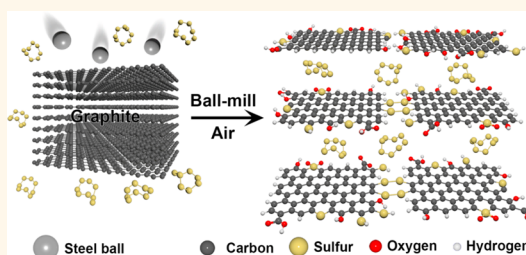


Sulfur–Graphene Nanostructured Cathodes *via* Ball-Milling for High-Performance Lithium–Sulfur Batteries

Jiantie Xu,^{†,‡} Jianglan Shui,[‡] Jianli Wang,^{†,§} Min Wang,[‡] Hua-Kun Liu,[†] Shi Xue Dou,^{*,†} In-Yup Jeon,[⊥] Jeong-Min Seo,[⊥] Jong-Beom Baek,^{*,⊥} and Liming Dai^{*,‡}

[†]Institute for Superconducting and Electronic Materials, University of Wollongong, Wollongong, NSW 2522, Australia, [‡]Department of Macromolecular Science and Engineering, School of Engineering, Case Western Reserve University, Cleveland, Ohio 44106, United States, [§]Bragg Institute, Australian Nuclear Science and Technology Organization, Lucas Heights, New South Wales 2234, Australia, and [⊥]School of Energy and Chemical Engineering/Low-Dimensional Carbon Materials Center, Ulsan National Institute of Science and Technology (UNIST), Banyeon, Ulsan 689-798, South Korea

ABSTRACT Although much progress has been made to develop high-performance lithium–sulfur batteries (LSBs), the reported physical or chemical routes to sulfur cathode materials are often multistep/complex and even involve environmentally hazardous reagents, and hence are infeasible for mass production. Here, we report a simple ball-milling technique to combine both the physical and chemical routes into a one-step process for low-cost, scalable, and eco-friendly production of graphene nanoplatelets (GnPs) edge-functionalized with sulfur (S-GnPs) as highly efficient LSB cathode materials of practical significance. LSBs based on the S-GnP cathode materials, produced by ball-milling 70 wt % sulfur and 30 wt % graphite, delivered a high initial reversible capacity of 1265.3 mAh g⁻¹ at 0.1 C in the voltage range of 1.5–3.0 V with an excellent rate capability, followed by a high reversible capacity of 966.1 mAh g⁻¹ at 2 C with a low capacity decay rate of 0.099% per cycle over 500 cycles, outperformed the current state-of-the-art cathode materials for LSBs. The observed excellent electrochemical performance can be attributed to a 3D “sandwich-like” structure of S-GnPs with an enhanced ionic conductivity and lithium insertion/extraction capacity during the discharge–charge process. Furthermore, a low-cost porous carbon paper pyrolyzed from common filter paper was inserted between the 0.75–0.3GnP electrode and porous polypropylene film separator to reduce/eliminate the dissolution of physically adsorbed polysulfide into the electrolyte and subsequent cross-deposition on the anode, leading to further improved capacity and cycling stability.



KEYWORDS: sulfur-graphene nanoplatelets · lithium sulfur batteries · ball milling · carbon paper

Because of their high energy density and long cycle life, lithium ion batteries (LIBs) have been widely used as the state-of-the-art energy storage devices in various portable and smart devices, including cell phones, MP3 devices, cameras, and laptops.^{1,2} Nevertheless, the specific capacities that can be obtained from current cathode materials for LIBs are insufficient to meet the ever increasing requirements for electrical vehicle (EV) and other energy-demanding applications. In comparison with the current state-of-the-art cathode materials, such as lithium metal oxides (140–200 mAh g⁻¹ and 500–700 Wh kg⁻¹) and lithium metal phosphates (140–190 mAh g⁻¹ and 560–800 Wh kg⁻¹), sulfur has recently received considerable attention as the cathode material for

lithium–sulfur batteries (LSBs) because of its much higher theoretical capacity (~1675 mAh g⁻¹) and energy density (~2600 Wh kg⁻¹).³ This, together with its low cost, earth abundance, and eco-friendliness, makes sulfur as one of the most promising cathode materials for next generation LSBs. However, sulfur-based cathode materials are still suffered from multiple drawbacks, including (1) the low electrical conductivity of sulfur S₈ (5 × 10⁻³⁰ S cm⁻¹ at 25 °C); (2) the large volume (~76%) and morphology changes of sulfur electrodes during the discharge–charge process; and (3) the easiness with which intermediate products (*e.g.*, lithium polysulfides, Li₂S_{4–8}, Li₂S₂, Li₂S) can be dissolved (Li₂S_{4–8}) into the electrolyte solution or deposited (Li₂S₂, Li₂S) on the lithium

* Address correspondence to
liming.dai@case.edu,
jbbak@unist.ac.kr,
shi_dou@uow.edu.au.

Received for review August 25, 2014
and accepted October 7, 2014.

Published online October 07, 2014
10.1021/nn5047585

© 2014 American Chemical Society

anode surface to increase the resistance and shorten the cycle life.^{4,5}

To overcome the above-mentioned obstacles, carbon based materials with various hierarchical structures, including meso-/microporous carbons,^{6–11} hollow carbon spheres,^{12–14} carbon nanotubes/nanofibers,^{15–19} graphene derivatives,^{20–30} and flexible carbon membranes,³¹ have been developed as conductive and structurally stable supports for compositing with sulfur. Meanwhile, coating the sulfur cathodes with appropriate polymers (e.g., conducting polymers) was demonstrated to not only effectively eliminate the dissolution of sulfur into the electrolyte solution but also reduce volume expansion of the sulfur electrode, leading to enhanced cycling stability.^{32–37} In addition, other physical and chemical routes have also been devised for the preparation of LSB cathode materials from sulfur composites with carbon materials or polymers. Examples include LSB cathodes based on sulfur mixed with either mesoporous single-walled carbon nanotube (SWCNT)-graphene¹⁸ or three-dimensional (3D) “sandwich-like” cetyltrimethylammonium bromide (CTAB)-graphene oxide (GO) hybrids (up to 800 mAh g⁻¹ at 6 C with a low decay rate of 0.039% per cycle over 1500 cycles),²⁵ a sulfur-graphene composite with ~63.6 wt % sulfur uniformly coated on graphene sheets through reduction of GO with concomitant sulfurization (440 mAh g⁻¹ after 500 cycles at 0.75 C),²² and polyvinylpyrrolidone (PVP)-encapsulated hollow S nanospheres (i.e., S@PVP nanospheres) from the reaction of Na₂S₂O₃ and HCl in an aqueous of PVP (849 mAh g⁻¹ at 2 C with a capacity decay of 0.046% per cycle over 1000 cycles at 0.5 C).³⁵ Although much progress has been made, the capacities and rate capability still need to be improved for practical applications. Furthermore, most of the reported physical and chemical routes to sulfur composites are multistep and complex, and hence too expensive for mass production; they often involve environmentally hazardous reagents (e.g., strong acids for GO production by Hummers' method).³⁸

We have recently developed a simple, low-cost, but effective and eco-friendly, ball-milling method for large-scale production of various graphene nanoplatelets (GnPs) edge-functionalized with different moieties without any basal-plane damage, and hence good electrical/thermal conductivities.^{39–42} By ball-milling graphite in the presence of sulfur (Figures S1 and S3, Supporting Information), we demonstrated in the present study that sulfur could edge-selectively functionalize GnPs (S-GnPs) with a concomitant homogeneous adsorption on and within the GnP structure, leading to highly efficient LSB cathode materials. Thus, the ball-milling technique has effectively combined both the physical and chemical routes into one-step process for low-cost, scalable, and eco-friendly production of highly efficient LSB cathode materials of

practical significance. We further found that LSBs based on the S-GnP cathode materials, produced by ball-milling 70 wt % sulfur and 30 wt % graphite (denoted as 0.7S-0.3GnP), delivered a high initial reversible capacity of 1265.3 mAh g⁻¹ at 0.1 C in the voltage range of 1.5–3.0 V with an excellent rate capability, followed by a high reversible capacity of 966.1 mAh g⁻¹ at 2 C with a low capacity decay rate of 0.099% per cycle over 500 cycles. Both the initial and reversible capacities observed for the 0.7S-0.3GnP are outstanding and attributable to its 3D porous “sandwich-like” structure from 3D self-assembling of the edge-functionalized S-GnPs (*vide infra*), leading to enhanced ionic conductivity and lithium insertion/extraction capacity during the discharge–charge process. To reduce/eliminate the dissolution of physically adsorbed polysulfide into the electrolyte and subsequent cross-deposition on the anode,^{29,43–46} we inserted a porous carbon paper pyrolyzed from common filter paper between the 0.7S-0.3GnP electrode and the porous polypropylene film separator (Supporting Information), which further improved the capacity and cycling stability.

RESULTS AND DISCUSSION

Figure 1a shows the schematic representation of the S-GnP preparation. Briefly, predetermined amounts of commercial graphite and sulfur were placed into a stainless steel jar containing stainless steel balls and sealed under argon for agitating at 500 rpm for 48 h in a planetary ball-mill machine (TCL, USA). The resultant product was designated as xS-yGnP (x and y represent the weight percentage of S and graphite, respectively, in the starting material. As we shall see later, the cell performance is well correlated to the starting stoichiometry, which, therefore, is used for the sample denotation). Figure 1b–e reproduces field emission scanning electron microscope (FE-SEM) images of the S-GnP samples with different sulfur loadings from 50 to 80 wt %, which show large particles of ~3–10 μm in size with a similar morphology to that of sulfur (Figure S1a) but different from the “plate-like” graphite (Figure S1b).

More close examination under a higher magnification (Figure 1f–i) revealed a morphological change from the “sulfur-like” bulk particles (Figure 1f, 0.5S-0.5GnP), through randomly distributed fragments with meso-/macropores (Figure 1g, 0.6S-0.4GnP) and “sandwich-like” layered meso-/macropores (Figure 1h, 0.7S-0.3GnP), to a uniform meso-/macroporous structure (Figure 1i, 0.8S-0.2GnP), indicating that the presence of sulfur in the ball-milled graphite facilitated the formation of 3D nanostructured carbon foams, presumably due to the strong S–S interaction between the edges of the functionalized S-GnP nanoplatelets. At a low sulfur content, the interaction between the edge S functionalities is not strong enough to arrange the S-GnPs into an ordered self-assembly, and hence the observed randomly distributed fragments in

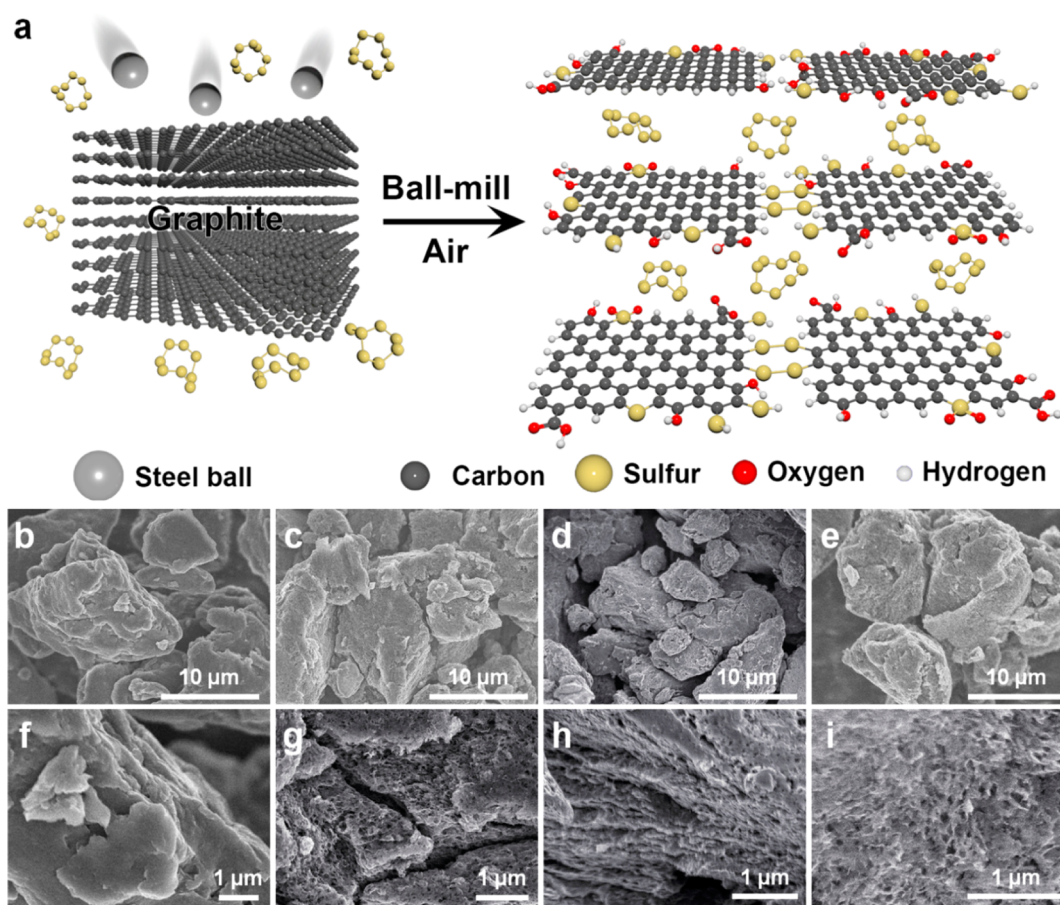


Figure 1. (a) Schematic representation of the S-GnP preparation; and FE-SEM images at different magnifications for samples with different starting compositions: (b, f) 0.5S-0.5GnP; (c, g) 0.6S-0.4GnP; (d, h) 0.7S-0.3GnP; and (e, i) 0.8S-0.2GnP.

Figure 1f and g. In contrast, an excessive amount of sulfur can also cause detrimental effects on the self-assembling induced by the S–S interaction as the presence of excessive sulfur particles (*cf.* Figure 2) between the S-GnP nanoplatelets could physically prevent the formation of an ordered assembly (Figure 1i). Therefore, it is a delicate balance between the edge-S interaction and the amount of sulfur in the S-GnP sample that makes the 0.7S-0.3GnP to show the “sandwich-like” layered meso-/macroporous morphology (Figure 1h). While the edge-functionalization without the basal plane damage would ensure good electrical/thermal conductivities for the resultant 3D network, the meso-/macroporous structures in both the “sandwich-like” and “foam-like” S-GnPs with a relatively large specific surface area ($138.1\text{--}182.6\text{ m}^2\text{ g}^{-1}$, Table S1) could allow for an efficient sulfur dispersion between the mechanically-stable GnP networks to alleviate the volume expansion/shrinkage of sulfur even during repeated discharge–charge cycles (*vide infra*).

Figure 2a and b shows the typical bright field (BF) and high angle annular dark field (DF) STEM images for 0.7S-0.3GnP with the corresponding selected area electron diffraction (SAED) patterns (inset of Figure 2a), while Figure 2c reproduces a secondary electron SE

STEM image with the surface sulfur particles being clearly evident. Figure 2a–c, together with the corresponding SAED pattern (inset of Figure 2a), show codeposition of $\sim 10\text{ nm}$ sulfur particles and amorphous sulfur into the GnP multilayer structure. As expected, the energy dispersive X-ray (EDX) spectrum given in Figure 2e shows the presence of dominate peaks for C and S (note, Cu is from the TEM carbon grid, while Fe and Co could come from the ball-milling reactor/balls).

We further carried out the energy dispersive spectroscopic (EDS) mapping (Figure 2f). As shown in Figure 2g–i, carbon, oxygen and sulfur all uniformly distributed throughout the sample. The observed homogeneous distribution of sulfur indicates the homogeneous adsorption/intercalation of sulfur on/into the GnPs, as mentioned above. The presence of oxygen is due to the post-ballmilling conversion of certain reactive edge-sulfur and carbon species into oxygen-containing functional groups (*e.g.*, $-\text{OH}$, $-\text{SO}_2$, $-\text{COOH}$, $-\text{SO}_3\text{H}$) through spontaneous reactions with oxygen/moisture in air upon opening the ball-milling reactor.⁴² To further investigate chemical structures of the S-GnP samples, we performed X-ray photoelectron spectroscopic (XPS) measurements. As expected, XPS survey spectra for all

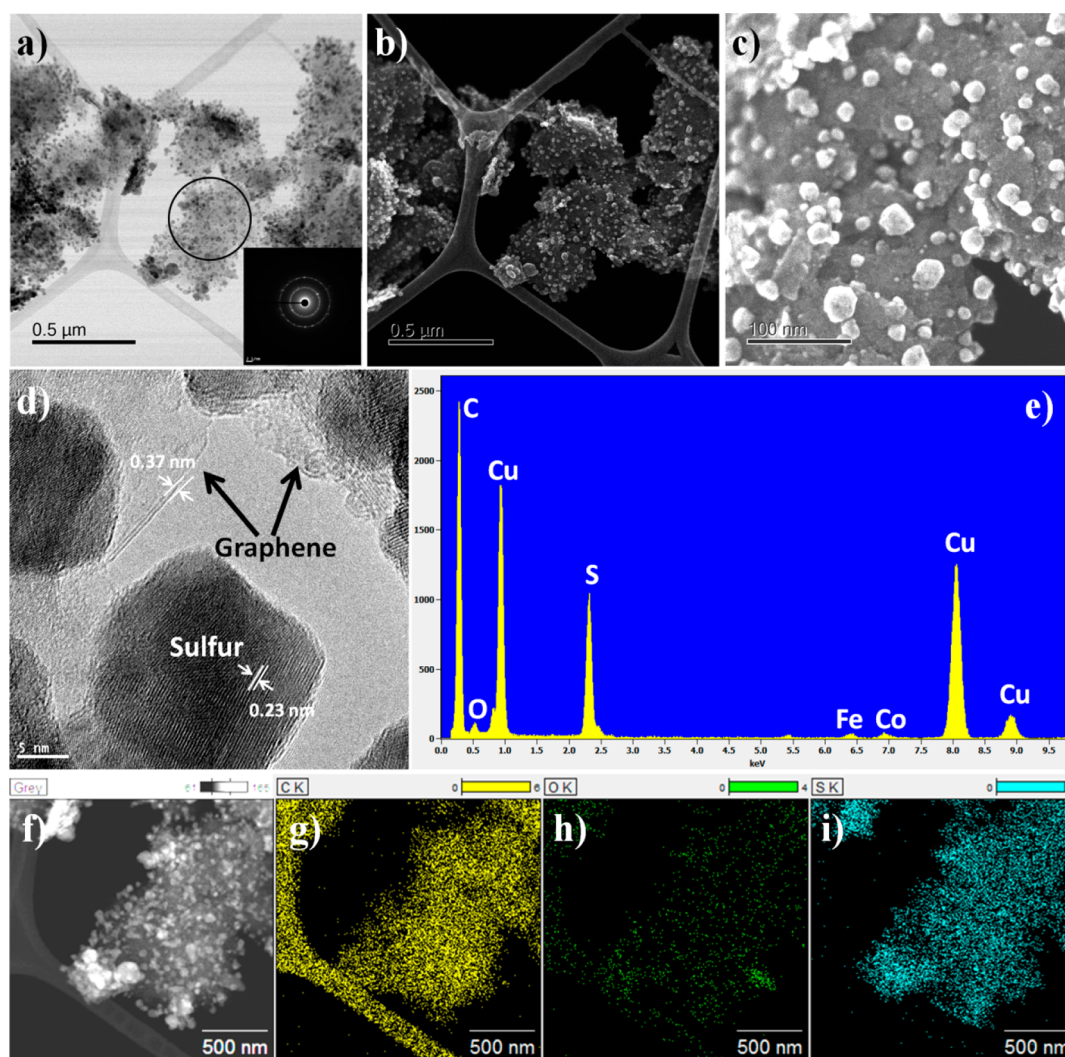


Figure 2. STEM images of 0.7S-0.3GnP: (a) bright field (BF) image. Inset is the selected area electron diffraction (SAED) pattern; (b) high angle annular dark field (HAADF) STEM images; (c) SE STEM image; (d) high-resolution TEM image of graphitic layers and single crystal sulfur (arrows); (e) energy dispersive X-ray (EDX) spectroscopy; (f) HAADF STEM image. Element mappings from (f): (g) carbon; (h) oxygen and (i) sulfur.

of the S-GnPs showed O 1s, C 1s, S 2s, and S 2p peaks at ~ 534 , ~ 285 , ~ 229 , and ~ 165 eV, respectively (Figure 3a). The high-resolution XPS C 1s, O 1s and S 2p spectra of the 0.7S-0.3GnP sample were shown in Figure S2a–c, respectively. As can be seen in Figure S2a, the C 1s peak can be deconvoluted into three peaks attributable to C–C bond at 285.1 eV, C–OH and C–S at 286.1 eV, and O=C–OH at 289.6 eV, while the corresponding O 1s spectrum shows O=C–OH and C–OH peaks at 532.2 and 533.9 eV, respectively (Figure S2b). The S 2p peak was well fitted to C–SO₃ at 168.3 eV and C–S at 165.2/164.3 eV (Figure S2c).⁴²

Thermogravimetric analyses (TGA) were performed under argon atmosphere to estimate the sulfur content in the S-GnP samples. Figure 3b shows significant weight losses over 200–500 °C for all of the S-GnP samples, due, most probably, to the evaporation of physically adsorbed sulfur. Up to 700 °C, the non-stoichiometric weight losses for the S-GnP samples

were 44.4% (0.5S-0.5GnP), 55.6% (0.6S-0.4GnP), 65.5% (0.7S-0.3GnP), and 75.8% (0.8S-0.2GnP), indicating that about 4 wt % (Table S2) sulfur has been chemically edge-functionalized on the S-GnPs. While the edge-functionalization of GnPs by ball milling in general has been verified in our previous studies,^{39–42} we tried to further confirm the edge-functionalization of sulfur by chemically and physically removing sulfur from the 0.7S-0.3GnP. The 0.7S-0.3GnP was Soxhlet extracted with carbon disulfide (CS₂) for several days to chemically remove sulfur. In the physical method, 0.7S-0.3GnP was heated up to 400 or 700 °C under argon for 2 h (*cf.* Figure S3). Subsequently, these samples were washed with 1 M HCl, and the final products were designed as 0.7S-0.3GnP-CS₂-1 M HCl and 0.7S-0.3GnP-400 or 700 °C-1 M HCl. The HCl washing will not only remove physically adsorbed S but also Fe residues, if any, from the ball-milling reactor/balls.

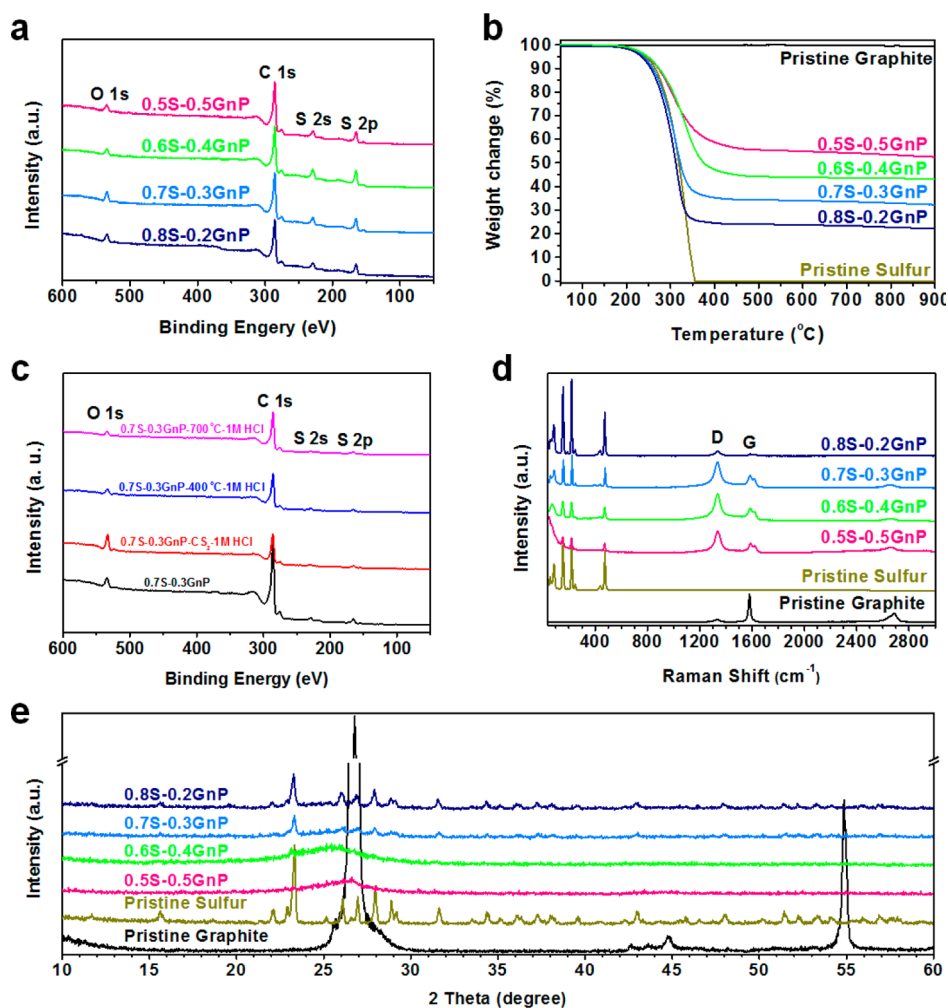


Figure 3. (a) X-ray photoelectron spectroscopy (XPS) for the S-GnPs; (b) thermogravimetric analysis (TGA) for the S-GnPs, graphite and sulfur; (c) XPS for the 0.7S-0.3GnP, 0.7S-0.3GnP-CS₂-1 M HCl, 0.7S-0.3GnP-400 °C-1 M HCl and 0.7S-0.3GnP-700 °C-1 M HCl (see text); (d) Raman spectroscopy for the S-GnPs, graphite, and sulfur; and (e) X-ray diffraction (XRD) patterns for the S-GnPs, graphite, and sulfur.

As shown in Figure S4, the XRD pattern of 0.7S-0.3GnP revealed characteristic peaks for the crystalline sulfur without the graphitic peak, indicating a complete exfoliation for the graphite (*cf.* Figure 3e). Upon CS₂ treatment or heating up to 400 or 700 °C, all the sulfur peaks disappeared, whereas the typical graphitic carbon peak (*cf.* Figure 3e) appeared (Figure S4), indicating that the exfoliated GnP partially restacked during the heat treatment due to the removal of the physically adsorbed sulfur. However, the presence of the XPS S peaks in Figures 3c, S2f,i,l, along with sulfur in elemental EDS mappings (Figures S5i and S6i), for 0.7S-0.3GnP-CS₂-1 M HCl and 0.7S-0.3GnP-700 °C-1 M HCl clearly indicates that a considerable amount (~3.8 at. %, Table S2) of sulfur have been strongly bonded into the carbon network through the C–S and C–SO₃ bonds, apart from those physically adsorbed sulfur.

Figure 3d shows typical Raman spectra for the pristine graphite, sulfur, and S-GnPs. A comparison of spectra for the S-GnPs to that of sulfur in Figure 3d

indicates the sulfur origin for those peaks in the range of 50–525 cm⁻¹. In addition, the S-GnP samples exhibited two peaks at ~1330 and ~1600 cm⁻¹ characteristic of the D and G bands, respectively.^{39–42} For all the S-GnPs, the intensity of the D band is higher than that of the G band due to the presence of defects induced by S-doping. Figure 3d further shows that the relative peak intensities of the sulfur peaks to the GnP peaks increased with increasing mass ratio of S/GnP. As shown in Figure 3d and Figure S7, the G band for all of the S-GnP samples can be fitted into two subpeaks (A and B in Figure S7), indicating the successful doping of S heteroatoms into the carbon networks, as is the case for N-doped graphene sheets.⁴⁷

Figure 3e shows X-ray diffraction (XRD) patterns of the pristine graphite, sulfur, and S-GnPs. As expected, the pristine graphite exhibited a prominent (002) peak at 26.5°, corresponding to an interlayer *d*-spacing of 0.34 nm, as well as two characterized peaks ((101) peak at 44.8° and (004) peak at 54.8°).⁴⁸ The salient feature to note is that the ball-milling caused a high degree of

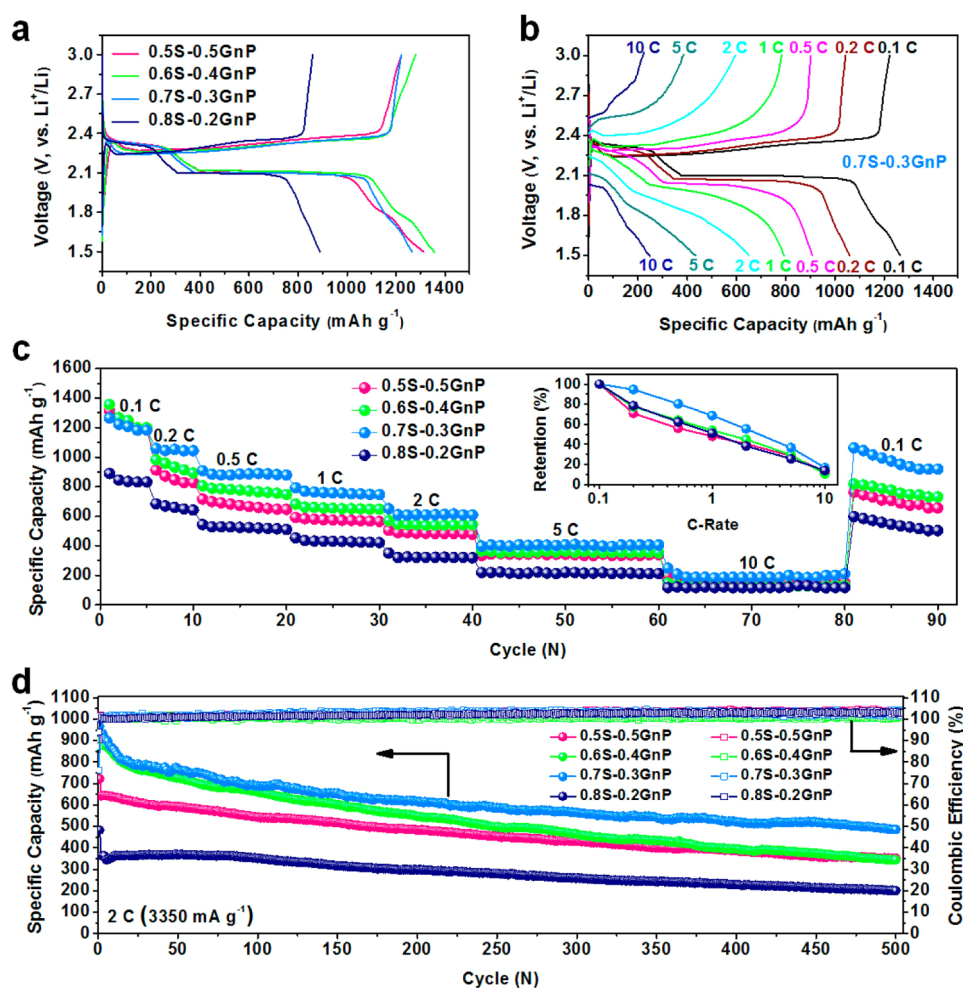


Figure 4. (a) Discharge–charge profiles of S-GnPs at 0.1 C; (b) discharge–charge profiles for 0.75S-0.3GnP at various C-rates; (c) rate capabilities of S-GnPs, with the inset showing the percentage capacity retention as a function of the C-rate; and (d) cycling performance of S-GnPs at 2 C (3350 mA g^{-1}) in the voltage range of 1.5–3.0 V.

exfoliation, as reflected by the dramatic reduction in intensity for graphitic peaks, along with a concomitant down-shift of the (002) band with increasing sulfur content, in a good consistence with the Raman results (Figure 3d). The almost fully exfoliated S-GnPs with a large surface area, good electrical conductivity, and meso-/micropores are ideal characteristics for LSB cathode materials, as described below.

Figure 4a shows typical discharge–charge profiles for the S-GnP cathodes at 0.1 C over 1.5–3.0 V. During the discharge process, two plateaus at ~ 2.35 and ~ 2.10 V were seen for all of the S-GnP samples, corresponding to the intercalation of lithium into S_8 to form a long chain (Li_2S_x , $2 \leq x \leq 4$) and short chain (Li_2S_x , $1 \leq x \leq 2$) of lithium polysulfides, respectively. The discharge–charge profiles for 0.75S-0.3GnP at various C-rates are given in Figure 4b, which shows increasingly shortened discharge–charge plateaus with increasing C-rate due to electrode polarization, in agreement with previous reports.^{7,8} To test the rate and cycling performance, we discharged and charged LSBs based on the S-GnP cathodes for 90 cycles in the

voltage range of 1.5–3.0 V at C-rates from 0.1 to 10 C (Figure 4c). As can be seen, the 0.6S-0.4GnP cathode showed the highest initial discharge capacity of $1356.3 \text{ mA h g}^{-1}$ at 0.1 C, followed by the 0.5S-0.5GnP ($1311.7 \text{ mA h g}^{-1}$), 0.7S-0.3GnP ($1265.3 \text{ mA h g}^{-1}$), and 0.8S-0.2GnP ($889.5 \text{ mA h g}^{-1}$). By increasing the C rate from 0.2 to 10 C, however, the 0.7S-0.3GnP cathode showed the highest reversible capacity and rate capability (inset of Figure 4c) among all the S-GnPs studied in this work. The average discharge capacities of the 0.7S-0.3GnP cathode at 0.2, 0.5, 1, 2, 5 and 10 C were 1043.1, 885.6, 756.8, 610.4, 404.8, and $186.5 \text{ mA h g}^{-1}$, respectively. When the C-rate was reduced back to 0.1 C after 80 cycles, the 0.7S-0.3GnP cathode can still deliver a higher reversible discharge capacity of $1063.2 \text{ mA h g}^{-1}$ than those of 0.5S-0.5GnP ($762.4 \text{ mA h g}^{-1}$), 0.6S-0.4GnP ($817.8 \text{ mA h g}^{-1}$), and 0.8S-0.2GnP ($598.1 \text{ mA h g}^{-1}$).

The excellent electrochemical stability of 0.7S-0.3GnP was also supported by cyclic voltammetry (CV) curves in Figure S8a, which shows highly overlapping CV curves over 4 cycles at 0.1 mV s^{-1} with well-defined and strong

redox peaks even after 90 cycles (Figure S8a). To investigate the kinetics of the S-GnP cathodes, we compared the electrochemical impedance spectroscopic (EIS) results for the cells cycled over 90 cycles. As shown in Figure S8b, the impedance curves for all of the S-GnP samples exhibited two apparent semicircles in the high and medium frequency regions, attributable to the lithium ion diffusion resistance through the electrolyte (R_e) (intercept of the first semicircle), the solid electrolyte interface (SEI) film resistance (R_s) (diameter of the first semicircle), and the charge transfer resistance (R_{ct}) (diameter of the second semicircle). The $\sim 45^\circ$ inclined line in the low-frequency range corresponds to a Warburg impedance.⁴⁹ The equivalent circuit model (inset of Figure S8b) was constructed to analyze the impedance spectra. The fitting results from this model are listed in Table S3. The lowest R_{ct} (79.9 Ω) and R_s (34.5 Ω) seen in Table S3 indicate the highest ionic conductivity for 0.7S-0.3GnP among all of the S-GnP samples investigated in the present study.

The S-GnP cathodes were further subjected to testing the relatively long cycling performance at 2 C in the voltage range of 1.5–3.0 V. Figure 4d shows initial discharge capacities of 966.1 mAh g⁻¹ (0.7S-0.3GnP), 919.9 mAh g⁻¹ (0.6S-0.4GnP), 722.7 mAh g⁻¹ (0.5S-0.5GnP), and 483.2 mAh g⁻¹ (0.8S-0.2GnP). After 500 cycles, these S-GnP cells can maintain discharge capacities of 485.6 mAh g⁻¹ (0.7S-0.3GnP), 352.9 mAh g⁻¹ (0.5S-0.5GnP), 344.8 mAh g⁻¹ (0.6S-0.4GnP), and 200.2 mAh g⁻¹ (0.8S-0.2GnP) with the initial capacity retentions of 50.3, 48.8, 37.5, and 41.4%, corresponding to the capacity decay rate of 0.099, 0.102, 0.125, and 0.117% per cycle, respectively. Despite their differences in the capacity and capacity retention, all of the S-GnP electrodes showed high Coulombic efficiencies around 100% due to their excellent structural stability during each of the discharge–charge cycles. Among all of the S-GnP cathodes, the 0.7S-0.3GnP showed the highest capacity and capacity retention at 2 C over 500 cycles, outperformed the current state-of-the-art cathode materials for LSBs,^{22,25,35} due to its unique 3D porous “sandwich-like” structure (cf. Figure 1h) with a relatively large surface area GnP (Table S1, 162.3 m² g⁻¹), low charge transfer resistance (Table S3, 79.9 Ω), low SEI resistance (Table S3, 34.5 Ω), high electronic conductivity (Table S5, 1.63×10^{-4} S cm⁻¹) and high sulfur uptake (Figure S9, ~ 1.5 g cm⁻³ tap density). Nevertheless, the spin redistribution induced by S-doping^{41,42} could also contribute to the excellent cathodic performance of the S-GnP samples. Furthermore, the 0.7S-0.3GnP with ~ 70 wt % sulfur uptake and a 1.5 g cm⁻³ high tap density could provide an areal capacity of (1–2 mAh cm⁻² at 2 C), comparable to the corresponding reported data,^{50–52} to meet the ever-increasing demand of high volumetric capacity for LSBs.

To further test the effects of the sulfur edge functionality and “sandwich-like” mesoporous structure on

the electrochemical performance of the 0.7S-0.3GnP, we prepared a reference sample by physically mixing 70 wt % sulfur with 30 wt % GnP (designated as 70 wt % S-30 wt % GnP), in which the GnP was obtained through the same ball-milling procedure as for the S-GnP with only graphite as the starting material. We compared the electrochemical performance of 0.7S-0.3GnP, 70 wt % S-30 wt % GnP, and GnP, respectively. As shown in Figure 5a and b, the 0.7S-0.3GnP showed significantly higher capacity and rate capability than both the 70 wt % S-30 wt % GnP, and GnP (Figure S10), indicating, once again, the important contributions of the sulfur edge functionality and “sandwich-like” mesoporous structure induced by the edge-doping with S to improve electrochemical performance of the 0.7S-0.3GnP sample.

To reduce/eliminate the dissolution of physically adsorbed polysulfide into the electrolyte and subsequent cross-deposition on the anode,^{29,43–46} especially associated with crystal sulfur particles on the surface of 0.7S-0.3GnP (Figure 2b and c), we inserted an amorphous porous carbon paper pyrolyzed from common filter paper⁵⁰ (Figure S11a) between the porous polypropylene film separator (Supporting Information) and the 0.7S-0.3GnP electrode.

The performance of the cell based on 0.7S-0.3GnP with the carbon paper (0.7S-0.3GnP-CP) was included in Figure 5 for comparison. As can be seen, the 0.7S-0.3GnP-CP exhibited similar electrochemical behavior as the 0.7S-0.3GnP (Figures 5a and S12), but with much higher specific capacities. As also shown in Figure 5a, the discharge curve for the 0.7S-0.3GnP-CP exhibited a long high potential plateau with a capacity of ~ 300 mAh g⁻¹ ($S_8 \rightarrow Li_2S_8$) and a slope with a capacity of ~ 210 mAh g⁻¹ ($Li_2S_8 \rightarrow Li_2S_6$ or Li_2S_4). The total capacity of ~ 510 mAh g⁻¹ is higher than the corresponding theoretical capacity (418 mAh g⁻¹, that is, ~ 209 mAh g⁻¹ for $S_8 \rightarrow Li_2S_8$ and $Li_2S_8 \rightarrow Li_2S_6$ or Li_2S_4 , respectively). The similar phenomenon has been previously reported with no clear rationalization,⁴³ which deserves more detailed studies in future work. Furthermore, the rate capability (Figure 5b) and long cycling performance (Figure 5c) of the 0.7S-0.3GnP-CP cathode were significantly improved with respect to 0.7S-0.3GnP cathode due to effective blocking of polysulfide intermediates, if any, by the microstructured carbon paper (Figure S11b–d) while retaining the efficient electrolyte diffusion.

As shown in Figure 5c, the 0.7S-0.3GnP-CP cathode delivered an initial discharge capacity of 970.9 mAh g⁻¹ (966.1 mAh g⁻¹, 0.7S-0.3GnP) at 2 C. After 500 cycles, the 0.7S-0.3GnP-CP cathode maintained the capacity of 679.7 mAh g⁻¹ with a capacity retention of 70.0% and $\sim 100\%$ average Coulombic efficiency (50.3 and $\sim 100\%$, 0.7S-0.3GnP). EIS results (Figure S13 and Table S5) and FE-SEM images (Figure S14) also support that the conductive carbon paper interlayer decreased the

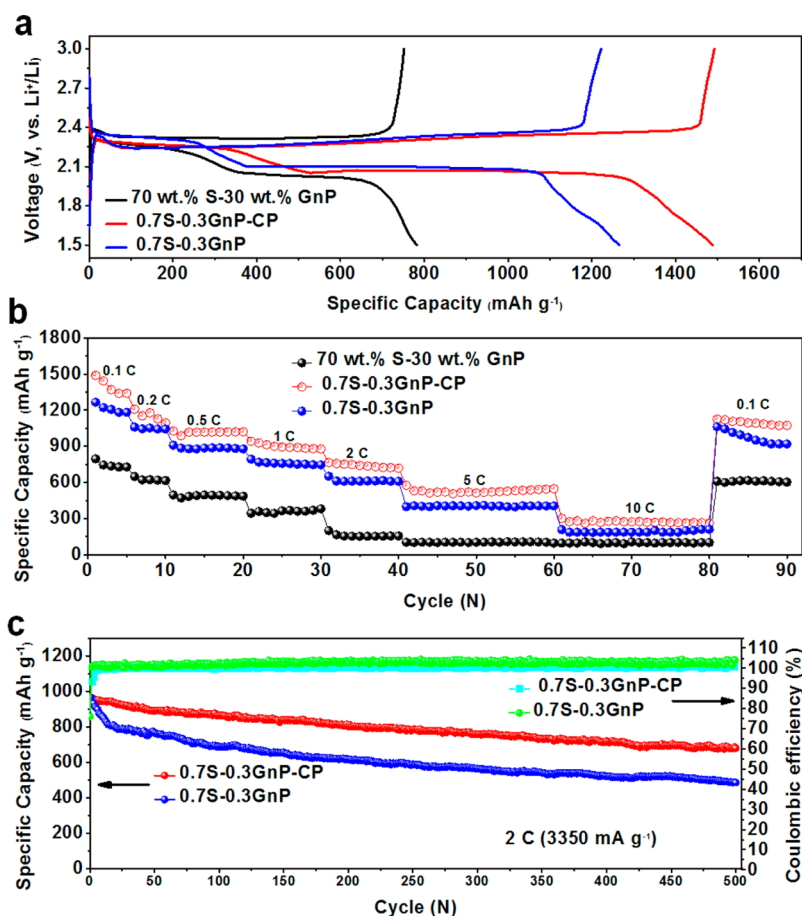


Figure 5. Electrochemical performance of 70 wt % S-30 wt % GnP, 0.7S-0.3GnP, 0.7S-0.3GnP-CP (carbon paper): (a) discharge–charge profiles of at 0.1 C; (b) rate capabilities and (c) cycling performance of S-GnPs at 2 C (3350 mA h g⁻¹) in the voltage range of 1.5–3.0 V.

interfacial resistance and stabilized polysulfides on the carbon paper or the surface of the cathode (Figure S14f), and thus effectively improved the electrochemical performance of the 0.7S-0.3GnP-CP cathode.

CONCLUSIONS

In summary, we have developed a simple one-step ball-milling method for low-cost and eco-friendly mass production of S-GnPs as efficient cathode materials (especially, 0.7S-0.3GnP) for lithium–sulfur batteries (LSBs). The 0.7S-0.3GnP cathode was demonstrated to deliver an initial reversible charge capacity of 1265.3 mA h g⁻¹ at 0.1 C in the voltage range of 1.5–3.0 V with a high reversible capacity of

966.1 mA h g⁻¹ at 2 C, a low capacity decay rate of 0.099% per cycle over 500 cycles, an excellent rate capability, attributable to the “sandwich-like” mesoporous structure induced by the edge-doping with sulfur. The superb cell performance was further improved by inserting an amorphous porous carbon paper pyrolyzed from common filter paper between the porous polypropylene film separator and the 0.7S-0.3GnP electrode to reduce/eliminate the dissolution of physically adsorbed polysulfide into the electrolyte and subsequent cross-deposition on the anode. These results clearly indicate that the newly developed S-GnP composites have a great potential for next generation high-performance LSBs.

EXPERIMENTAL METHODS

Synthesis of S-Graphene Nanoplatelet (GnP) Composites. To start with, predetermined amounts of commercial graphite and sulfur were placed into a stainless steel jar containing stainless steel balls (500 g, diameter 5 mm). Then, the jar was sealed and charged with argon after several charging–discharging cycles. Thereafter, the jar was fixed in a planetary ball-mill machine (TCI, USA) and agitated at 500 rpm for 48 h. Finally, the resultant powders were obtained and denoted as xS-yGnP (here, x and y

represent the weight percentage of S and graphite, respectively, in the starting material; for example, 0.7S-0.3GnP stands for ball-milling with 70 wt % sulfur and 30 wt % graphite in the starting materials). The xS-yGnP samples were further heated at 400 or 700 °C with a temperature ramp of 2 °C min⁻¹ in a tube furnace for 2 h under an argon flow (1000 s.c.c.m.) to remove physically adsorbed sulfur to produce the sample denoted as xS-yGnP-400 °C or xS-yGnP-700 °C. In order to get rid of any metallic impurities possibly from the ball-milling reactor and

steel balls, the xS-yGnP-400 °C or xS-yGnP-700 °C samples were further purified by washing with 1 M HCl (Figure S3) to obtain xS-yGnP-400 °C-1 M HCl or xS-yGnP-700 °C-1 M HCl samples. Along with the HCl washing, some of the resultant xS-yGnPs were also Soxhlet extracted with carbon disulfide (CS₂) to remove sulfur residues to investigate the effects of the physically adsorbed sulfur. The final product was freeze-dried at -120 °C under reduced pressure (0.05 mmHg) for 48 h to yield dark black powder. The obtained product was designated as xS-yGnP-CS₂-1 M HCl. Meanwhile, a GnP sample was prepared by the same ball-milling procedure as those for the S-GnP samples, but without sulfur being introduced into the starting material. The black carbon paper was generated from the filter paper (Hangzhou Special Paper Industry Co., Ltd., China) pyrolyzed at 800 °C with a temperature ramp of 10 °C min⁻¹ in a tube furnace for 2 h under an argon flow (500 s.c.c.m.).

Characterization. The phase identification of S-GnP compounds was carried out by powder X-ray diffraction (XRD, GBC MMA 017). The morphology of S-GnP was characterized by field emission scanning electron microscopy (FE-SEM), using JSM-7500FA, respectively. Scanning transmission electron microscope (STEM) images were acquired on a probe-corrected JEOL ARM200F operated at 200 kV equipped with a cold field emission gun, a high resolution pole-piece, and a Centurio EDS detector with a collection solid angle of ~1 Sr. Images and EDS maps were acquired at a probe current of 90 pA. The elemental mapping was carried out by energy dispersive X-ray spectroscopy (EDS) using the JSM-7500FA. The sulfur content of the S-GnP composites was determined by thermogravimetric analysis (TGA, TA Instruments 2000) under argon over a temperature range of 25–900 °C with a temperature ramp of 10 °C min⁻¹. The specific surface area was measured using 15 point N₂ adsorption Brunauer–Emmett–Teller (BET) method using Quanta Chrome Nova 1000. X-ray photoelectron spectroscopy (XPS) measurements were carried out on a VG Scientific ESCA-LAB 2201XL instrument using aluminum K α X-ray radiation. Raman spectra were collected using a Raman spectrometer (Lab RAM HR, Horiba Jobin Yvon SAS). The electrical conductivity of xS-yGnP powders was measured with a Jandel RM3 four-point probe system at room temperature. Specimens used for the electrical conductivity measurements were disk-shaped pellets with 8 mm in diameter and 1.5 mm in thickness, which were also used for the tap density measurements.

Electrochemical Measurements. The electrochemical characterization of the S-GnP composites was carried out using coin cells. The electrodes were fabricated by blending the active material (e.g., xS-yGnPs, 70 wt % S-30 wt % GnP, and GnP) powders with acetylene black and polyvinylidene fluoride (PVDF) binder in a weight ratio of 8:1:1. *N*-Methyl-2-pyrrolidone (NMP) was used as the blending solvent for the mixture. The slurries were prepared using a Kurabo MAZERSTAR planetary mixer, model KK-250S, for 15 min. The obtained slurry was coated on an Al foil, dried at 50 °C for 48 h, and then pressed under moderate pressure. The electrodes were punched into in a round area with 2 mg cm⁻² of active material. 2032 coin-type cells were assembled in an Ar-filled glovebox by stacking the *as-prepared* electrode as the working electrode, with Li foil as the counter electrode and reference electrode, a porous polypropylene film as separator, and 1 M lithium bis(trifluoromethanesulfonyl)imide in 1,3-dioxolane (DOL)/dimethoxyethane (DME) (1:1, v/v), including 0.1 M LiNO₃, as the electrolyte. The cells were galvanostatically discharged and charged using an automatic battery testing system (Land, China) at various current densities in a voltage range of 1.5–3.0 V at room temperature. Electrochemical impedance spectroscopy (EIS) and cyclic voltammetry (CV) measurements were performed on a Biologic MVP 3 electrochemical workstation. Electrochemical impedance spectroscopy (EIS) measurements were performed over the frequency range of 10 mHz to 1 M Hz. Cyclic voltammogram measurements were performed at a scan rate of 0.1 mV s⁻¹ in a voltage range of 1.5–3.0 V. The specific capacity and the C-rate were calculated based on the mass of active material. On the basis of the TGA results shown in Figure 3b and Table S2, it was assumed that the physically adsorbed sulfur mass of 0.5S-0.5GnP, 0.6S-0.4GnP, 0.7S-0.3GnP, 0.8S-0.2GnP were 45, 55, 65, 75 wt %, respectively. As shown in Figure S10, the

contribution of the GnP to the total capacity is limited and thus is not taken in account.

Conflict of Interest: The authors declare no competing financial interest.

Acknowledgment. The authors are grateful for financial support from the Auto CRC 2020, the Air Force Office of Scientific Research (AFOSR) (FA9550-12-1-0037, FA-9550-12-1-0069), and the National Science Foundation (NSF) (NSF-AIR-IIP-1343270, NSF-DMR-1106160). The authors thank Dr. T. Silver and Dr. Zhian Zhang. The authors acknowledge use of the facilities (Australian Research Council (ARC) – Linkage, Infrastructure, Equipment and Facilities (LIEF) Grant (LE120100104)) and the assistance of Dr. Gilberto Casillas at the University of Wollongong Electron Microscopy Centre.

Supporting Information Available: Supplementary tables (Table S1–S5) and figures (Figures S1–S14). This material is available free of charge via the Internet at <http://pubs.acs.org>.

REFERENCES AND NOTES

- Goodenough, J. B.; Kim, Y. Challenges for Rechargeable Li Batteries. *Chem. Mater.* **2009**, *22*, 587–603.
- Etacheri, V.; Marom, R.; Elazari, R.; Salitra, G.; Aurbach, D. Challenges in the Development of Advanced Li-Ion Batteries: A Review. *Energy Environ. Sci.* **2011**, *4*, 3243–3262.
- Xu, J. T.; Dou, S. X.; Liu, H. K.; Dai, L. M. Cathode Materials for Next Generation Lithium Ion Batteries. *Nano Energy* **2013**, *2*, 439–442.
- Evers, S.; Nazar, L. F. New Approaches for High Energy Density Lithium–Sulfur Battery Cathodes. *Acc. Chem. Res.* **2012**, *46*, 1135–1143.
- Manthiram, A.; Fu, Y.; Su, Y.-S. Challenges and Prospects of Lithium–Sulfur Batteries. *Acc. Chem. Res.* **2012**, *46*, 1125–1134.
- Wang, J.; Chew, S.; Zhao, Z.; Ashraf, S.; Wexler, D.; Chen, J.; Ng, S.; Chou, S.; Liu, H. Sulfur–Mesoporous Carbon Composites in Conjunction with a Novel Ionic Liquid Electrolyte for Lithium Rechargeable Batteries. *Carbon* **2008**, *46*, 229–235.
- Ji, X.; Lee, K. T.; Nazar, L. F. A Highly Ordered Nanostructured Carbon–Sulphur Cathode for Lithium–Sulphur Batteries. *Nat. Mater.* **2009**, *8*, 500–506.
- Ji, X.; Evers, S.; Black, R.; Nazar, L. F. Stabilizing Lithium–Sulphur Cathodes using Polysulphide Reservoirs. *Nat. Commun.* **2011**, *2*, 325.
- Jayaprakash, N.; Shen, J.; Moganty, S. S.; Corona, A.; Archer, L. A. Porous Hollow Carbon@Sulfur Composites for High-Power Lithium–Sulfur Batteries. *Angew. Chem., Int. Ed.* **2011**, *50*, 5904–5908.
- Schuster, J.; He, G.; Mandlmeier, B.; Yim, T.; Lee, K. T.; Bein, T.; Nazar, L. F. Spherical Ordered Mesoporous Carbon Nanoparticles with High Porosity for Lithium–Sulfur Batteries. *Angew. Chem., Int. Ed.* **2012**, *51*, 3591–3595.
- Huang, C.; Xiao, J.; Shao, Y.; Zheng, J.; Bennett, W. D.; Lu, D.; Laxmikant, S. V.; Engelhard, M.; Ji, L.; Zhang, J. Manipulating Surface Reactions in Lithium–Sulphur Batteries Using Hybrid Anode Structures. *Nat. Commun.* **2014**, *5*, 3015.
- Zhang, B.; Qin, X.; Li, G.; Gao, X. Enhancement of Long Stability of Sulfur Cathode by Encapsulating Sulfur into Micropores of Carbon Spheres. *Energy Environ. Sci.* **2010**, *3*, 1531–1537.
- Zheng, G.; Yang, Y.; Cha, J. J.; Hong, S. S.; Cui, Y. Hollow Carbon Nanofiber-Encapsulated Sulfur Cathodes for High Specific Capacity Rechargeable Lithium Batteries. *Nano Lett.* **2011**, *11*, 4462–4467.
- Zhang, C. F.; Wu, H. B.; Yuan, C. Z.; Guo, Z. P.; Lou, X. W. Confining Sulfur in Double-Shelled Hollow Carbon Spheres for Lithium–Sulfur Batteries. *Angew. Chem., Int. Ed.* **2012**, *51*, 9592–9595.
- Yuan, L.; Yuan, H.; Qiu, X.; Chen, L.; Zhu, W. Improvement of Cycle Property of Sulfur-Coated Multi-Walled Carbon Nanotubes Composite Cathode for Lithium/Sulfur Batteries. *J. Power Sources* **2009**, *189*, 1141–1146.

16. Guo, J.; Xu, Y.; Wang, C. Sulfur-Impregnated Disordered Carbon Nanotubes Cathode for Lithium–Sulfur Batteries. *Nano Lett.* **2011**, *11*, 4288–4294.
17. Elazari, R.; Salitra, G.; Garsuch, A.; Panchenko, A.; Aurbach, D. Sulfur-Impregnated Activated Carbon Fiber Cloth as a Binder-Free Cathode for Rechargeable Li-S Batteries. *Adv. Mater.* **2011**, *23*, 5641–5644.
18. Zhao, M.-Q.; Liu, X.-F.; Zhang, Q.; Tian, G.-L.; Huang, J.-Q.; Zhu, W.; Wei, F. Graphene/Single-Walled Carbon Nanotube Hybrids: One-Step Catalytic Growth and Applications for High-Rate Li–S Batteries. *ACS Nano* **2012**, *6*, 10759–10769.
19. Lu, S.; Cheng, Y.; Wu, X.; Liu, J. Significantly Improved Long-Cycle Stability in High-Rate Li–S Batteries Enabled by Coaxial Graphene Wrapping over Sulfur-Coated Carbon Nanofibers. *Nano Lett.* **2013**, *13*, 2485–2489.
20. Wang, H.; Yang, Y.; Liang, Y.; Robinson, J. T.; Li, Y.; Jackson, A.; Cui, Y.; Dai, H. Graphene-Wrapped Sulfur Particles as a Rechargeable Lithium–Sulfur Battery Cathode Material with High Capacity and Cycling Stability. *Nano Lett.* **2011**, *11*, 2644–2647.
21. Ji, L.; Rao, M.; Zheng, H.; Zhang, L.; Li, Y.; Duan, W.; Guo, J.; Cairns, E. J.; Zhang, Y. Graphene Oxide as a Sulfur Immobilizer in High Performance Lithium/Sulfur Cells. *J. Am. Chem. Soc.* **2011**, *133*, 18522–18525.
22. Sun, H.; Xu, G.-L.; Xu, Y.-F.; Sun, S.-G.; Zhang, X.; Qiu, Y.; Yang, S. A Composite Material of Uniformly Dispersed Sulfur on Reduced Graphene Oxide: Aqueous One-pot Synthesis, Characterization and Excellent Performance as the Cathode in Rechargeable Lithium-Sulfur Batteries. *Nano Res.* **2012**, *5*, 726–738.
23. Zhou, G.; Yin, L.-C.; Wang, D.-W.; Li, L.; Pei, S.; Gentle, I. R.; Li, F.; Cheng, H.-M. Fibrous Hybrid of Graphene and Sulfur Nanocrystals for High-Performance Lithium–Sulfur Batteries. *ACS Nano* **2013**, *7*, 5367–5375.
24. Lin, T.; Tang, Y.; Wang, Y.; Bi, H.; Liu, Z.; Huang, F.; Xie, X.; Jiang, M. Scotch-Tape-Like Exfoliation of Graphite Assisted with Elemental Sulfur and Graphene-Sulfur Composites for High-Performance Lithium-Sulfur Batteries. *Energy Environ. Sci.* **2013**, *6*, 1283–1290.
25. Song, M.-K.; Zhang, Y.; Cairns, E. J. A Long-Life, High-Rate Lithium/Sulfur Cell: A Multifaceted Approach to Enhancing Cell Performance. *Nano Lett.* **2013**, *13*, 5891–5899.
26. Rong, J.; Ge, M.; Fang, X.; Zhou, C. Solution Ionic Strength Engineering As a Generic Strategy to Coat Graphene Oxide (GO) on Various Functional Particles and Its Application in High-Performance Lithium–Sulfur (Li–S) Batteries. *Nano Lett.* **2013**, *14*, 473–479.
27. Chen, R.; Zhao, T.; Lu, J.; Wu, F.; Li, L.; Chen, J.; Tan, G.; Ye, Y.; Amine, K. Graphene-Based Three-Dimensional Hierarchical Sandwich-type Architecture for High-Performance Li/S Batteries. *Nano Lett.* **2013**, *13*, 4642–4649.
28. Zhao, M.-Q.; Zhang, Q.; Huang, J.-Q.; Tian, G.-L.; Nie, J.-Q.; Peng, H.-J.; Wei, F. Unstacked Double-layer Templated Graphene for High-Rate Lithium–Sulphur Batteries. *Nat. Commun.* **2014**, *5*, 3410.
29. Zhou, G.; Pei, S.; Li, L.; Wang, D. W.; Wang, S.; Huang, K.; Yin, L. C.; Li, F.; Cheng, H. M. A Graphene–Pure-Sulfur Sandwich Structure for Ultrafast, Long-Life Lithium–Sulfur Batteries. *Adv. Mater.* **2014**, *26*, 625–631.
30. Lu, S.; Chen, Y.; Wu, X.; Wang, Z.; Li, Y. Three-Dimensional Sulfur/Graphene Multifunctional Hybrid Sponges for Lithium-Sulfur Batteries with Large Areal Mass Loading. *Sci. Rep.* **2014**, *4*, 4629.
31. Zhou, G.; Wang, D.-W.; Li, F.; Hou, P.-X.; Yin, L.; Liu, C.; Lu, G. Q. M.; Gentle, I. R.; Cheng, H.-M. A Flexible Nanostructured Sulphur–Carbon Nanotube Cathode with High Rate Performance for Li-S batteries. *Energy Environ. Sci.* **2012**, *5*, 8901–8906.
32. Wang, J.; Yang, J.; Xie, J.; Xu, N. A Novel Conductive Polymer–Sulfur Composite Cathode Material for Rechargeable Lithium Batteries. *Adv. Mater.* **2002**, *14*, 963–965.
33. Yang, Y.; Yu, G.; Cha, J. J.; Wu, H.; Vosgueritchian, M.; Yao, Y.; Bao, Z.; Cui, Y. Improving the Performance of Lithium–Sulfur Batteries by Conductive Polymer Coating. *ACS Nano* **2011**, *5*, 9187–9193.
34. Xiao, L.; Cao, Y.; Xiao, J.; Schwenzer, B.; Engelhard, M. H.; Saraf, L. V.; Nie, Z.; Exarhos, G. J.; Liu, J. A Soft Approach to Encapsulate Sulfur: Polyaniline Nanotubes for Lithium-Sulfur Batteries with Long Cycle Life. *Adv. Mater.* **2012**, *24*, 1176–1181.
35. Li, W.; Zheng, G.; Yang, Y.; Seh, Z. W.; Liu, N.; Cui, Y. High-Performance Hollow Sulfur Nanostructured Battery Cathode through a Scalable, Room Temperature, One-Step, Bottom-Up Approach. *Proc. Natl. Acad. Sci. U. S. A.* **2013**, *110*, 7148–7153.
36. Wang, L.; Dong, Z.; Wang, D.; Zhang, F.; Jin, J. Covalent Bond Glued Sulfur Nanosheet-Based Cathode Integration for Long-Cycle-Life Li–S Batteries. *Nano Lett.* **2013**, *13*, 6244–6250.
37. Li, W.; Zhang, Q.; Zheng, G.; Seh, Z. W.; Yao, H.; Cui, Y. Understanding the Role of Different Conductive Polymers in Improving the Nanostructured Sulfur Cathode Performance. *Nano Lett.* **2013**, *13*, 5534–5540.
38. Hummers, W. S., Jr; Offeman, R. E. Preparation of Graphitic Oxide. *J. Am. Chem. Soc.* **1958**, *80*, 1339–1339.
39. Jeon, I.-Y.; Shin, Y.-R.; Sohn, G.-J.; Choi, H.-J.; Bae, S.-Y.; Mahmood, J.; Jung, S.-M.; Seo, J.-M.; Kim, M.-J.; Chang, D. W. Edge-Carboxylated Graphene nanosheets via Ball milling. *Proc. Natl. Acad. Sci. U. S. A.* **2012**, *109*, 5588–5593.
40. Jeon, I.-Y.; Choi, H.-J.; Jung, S.-M.; Seo, J.-M.; Kim, M.-J.; Dai, L.; Baek, J.-B. Large-Scale Production of Edge-selectively Functionalized Graphene Nanoplatelets via Ball Milling and Their use as Metal-Free Electrocatalysts for Oxygen Reduction Reaction. *J. Am. Chem. Soc.* **2012**, *135*, 1386–1393.
41. Jeon, I.-Y.; Choi, H.-J.; Choi, M.; Seo, J.-M.; Jung, S.-M.; Kim, M.-J.; Zhang, S.; Zhang, L.; Xia, Z.; Dai, L. Facile, Scalable Synthesis of Edge-halogenated Graphene Nanoplatelets as Efficient Metal-Free Electrocatalysts for Oxygen Reduction Reaction. *Sci. Rep.* **2013**, *3*, 1810.
42. Jeon, I. Y.; Zhang, S.; Zhang, L.; Choi, H. J.; Seo, J. M.; Xia, Z.; Dai, L.; Baek, J. B. Edge-Selectively Sulfurized Graphene Nanoplatelets as Efficient Metal-Free Electrocatalysts for Oxygen Reduction Reaction: The Electron Spin Effect. *Adv. Mater.* **2013**, *25*, 6138–6145.
43. Su, Y.-S.; Manthiram, A. Lithium–Sulphur Batteries with a Microporous Carbon Paper as a Bifunctional Interlayer. *Nat. Commun.* **2012**, *3*, 1166.
44. Huang, C.; Xiao, J.; Shao, Y.; Zheng, J.; Bennett, W. D.; Lu, D.; Saraf, L. V.; Engelhard, M.; Ji, L.; Zhang, J. Manipulating Surface Reactions in Lithium–Sulphur Batteries using Hybrid Anode Structures. *Nat. Commun.* **2014**, *5*, 3015.
45. Vizintin, A.; Patel, M. U. M.; Genorio, B.; Dominko, R. Effective Separation of Lithium Anode and Sulfur Cathode in Lithium–Sulfur Batteries. *ChemElectroChem* **2014**, *1*, 1040–1045.
46. Yao, H.; Yan, K.; Li, W.; Zheng, G.; Kong, D.; Seh, Z. W.; Narasimhan, V. K.; Liang, Z.; Cui, Y. Improved Lithium–Sulfur Batteries with a Conductive Coating on the Separator to Prevent the Accumulation of Inactive S-Related Species at the Cathode–Separator Interface. *Energy Environ. Sci.* **2014** In press.
47. Deng, D.; Pan, X.; Yu, L.; Cui, Y.; Jiang, Y.; Qi, J.; Li, W.-X.; Fu, Q.; Ma, X.; Xue, Q.; Sun, G.; Bao, X. Toward N-Doped Graphene via Solvothermal Synthesis. *Chem. Mater.* **2011**, *23*, 1188–1193.
48. Choi, E.-K.; Jeon, I.-Y.; Oh, S.-J.; Baek, J.-B. “Direct” Grafting of Linear Macromolecular “Wedges” to the Edge of Pristine Graphite to Prepare Edge-Functionalized Graphene-Based Polymer Composites. *J. Mater. Chem.* **2010**, *20*, 10936–10942.
49. Xu, J. T.; Chou, S. L.; Gu, Q. F.; Liu, H. K.; Dou, S. X. The Effect of Different Binders on Electrochemical Properties of $\text{LiNi}_{1/3}\text{Mn}_{1/3}\text{Co}_{1/3}\text{O}_2$ Cathode Material in Lithium Ion Batteries. *J. Power Sources* **2013**, *225*, 172–178.
50. Xu, T.; Song, J.; Gordin, M. L.; Sohn, H.; Yu, Z.; Chen, S.; Wang, D. Mesoporous Carbon–Carbon Nanotube–Sulfur Composite Microspheres for High-Areal-Capacity Lithium–Sulfur

- Battery Cathodes. *ACS Appl. Mater. Interfaces* **2013**, *5*, 11355–11362.
51. Song, J.; Xu, T.; Gordin, M. L.; Zhu, P.; Lv, D.; Jiang, Y. B.; Chen, Y.; Duan, Y.; Wang, D. Nitrogen-Doped Mesoporous Carbon Promoted Chemical Adsorption of Sulfur and Fabrication of High-Areal-Capacity Sulfur Cathode with Exceptional Cycling Stability for Lithium-Sulfur Batteries. *Adv. Funct. Mater.* **2014**, *24*, 1243–1250.
52. Luo, W.; Wang, B.; Heron, C. G.; Allen, M. J.; Morre, J.; Maier, C. S.; Stickle, W. F.; Ji, X. Pyrolysis of Cellulose under Ammonia Leads to Nitrogen-Doped Nanoporous Carbon Generated through Methane Formation. *Nano Lett.* **2014**, *14*, 2225–2229.